Piezoelectric energy harvesting from vortex-induced vibration of a circular cylinder: Effect of Reynolds number

Mingjie Zhang[1], Chengyun Zhang[2], Abdessattar Abdelkefi[3], Haiyan Yu[4], Oleg Gaidai[5], Xiang Qin[2], Hongjun Zhu[6,*], Junlei Wang[2,]**

1. Department of Structural Engineering, Norwegian University of Science and Technology, 7491, Trondheim, Norway.

2. School of Mechanical and Power Engineering, Zhengzhou University, Zhengzhou 450000, China.

3. Department of Mechanical and Aerospace Engineering, New Mexico State University, Las Cruces, NM 88003, USA.

4. School of Civil Engineering, Dalian University of Technology, Dalian, 116024, China.

5. School of Naval Architecture and Offshore Engineering, Jiangsu University of Science and Technology, Zhenjiang, China

6. State Key Laboratory of Oil and Gas Reservoir Geology and Exploitation, Southwest Petroleum University, Chengdu 610500, China

*Corresponding author: Hongjun Zhu, Email: zhuhj@swpu.edu.cn;

**Corresponding author: Junlei Wang, Email: jlwang@zzu.edu.cn

Abstract

This study investigates the effects of the Reynolds number on the piezoelectric energy harvesting from vortex-induced vibrations (VIV) of a circular cylinder. The VIV-based piezoelectric energy harvester is simulated by a representative electro-aero-mechanical model, in which the aerodynamic force is represented by a model with amplitude-dependent aerodynamic parameters and an aerodynamic damping envelope model. The amplitude-dependent aerodynamic parameters at two typical Reynolds numbers are identified based on free vibration experiments and forced vibration numerical simulations, respectively. The aerodynamic damping envelope over a Reynolds number range of 500 ~ 33000 are identified based on the Reynolds number-dependent Griffin plot. Wind tunnel experiments are carried out to verify the accuracy of the electro-aero-mechanical model for the VIV-based piezoelectric energy harvester. A parametric study is then performed to investigate the Reynolds number effects on the bifurcation diagrams and maximum power output of a VIV-based piezoelectric energy harvester. It is demonstrated that the Reynolds number affects not only the levels of the harvested power, but also the global branches of the bifurcation diagram. The results also show that the performance of a VIV-based piezoelectric energy harvester is more sensitive to the Reynolds number for a case with low mechanical damping ratio.

Keywords: Vortex-induced vibration; Piezoelectric energy harvesting; Circular cylinder; Reynolds number; Experimental measurements

Nomenclature	
A	Vibration amplitude
A_{max}	Peak amplitude in the lock-in range
C_L'	Fluctuating lift coefficient
C_p	Capacitance
D	Cylinder diameter
F_y	Aerodynamic force in cross-flow direction
H_1^*	Aerodynamic damping parameter
H_4^*	Aerodynamic stiffness parameter
$H_{1,max}^*$	Aerodynamic damping envelope
I	Current
m	Mass per unit length (including structural mass and fluid added mass)
$m_a = \pi\rho D^2/4$	Potential fluid added mass
R	Electrical load resistance
$Re = \rho UD/\mu$	Reynolds number
St	Strouhal number
U	Wind speed
$U_r = 2\pi U/\omega_0 D$	Reduced wind speed
V	Voltage
y	Vertical displacement
ρ	Fluid mass density
ω_0	Natural frequency in rad/s
ξ_0	Mechanical damping ratio
$\alpha = m\xi_0/m_a$	Mass-damping parameter
μ	Viscosity
θ	Electromechanical coupling coefficient

1. Introduction

Energy harvesting technology has been recognized as a promising energy supplement to power low-energy consumption devices, e.g. wireless sensor networks, micro-electromechanical systems, and sensors on unmanned aerial vehicles, etc. [1-3]. Towards energy harvesting from ambient vibrations, various efforts have been paid to broaden the effective bandwidth of vibration energy harvesting, such as the using of multi-degree-of-freedom structures, employing mechanical nonlinearities, or combining some different energy harvesting principles including piezoelectric [4-6], electromagnetic [7], electrostatic [8, 9], triboelectric [10], and their combinations [11, 12].

Wind and water flow are ubiquitous sources in nature that have already been recognized as important renewable energy resources [13-15]. Traditional methods using windmill-like turbo-machineries or water turbines to collect energy from wind or water have proved that it is reasonable to scavenge high-speed flow energy [16, 17]. In addition, flow-induced vibrations (FIVs) are quite good ways to convert flow energy, particularly low-speed flow energy into mechanical vibratory energy which can be well employed during the design of energy harvesters [18-21].

Energy harvesting from FIVs is realized mainly based on three common aerodynamic phenomena, i.e., vortex-induced vibrations, galloping, and flutter [22-27]. For galloping and flutter, it is beneficial to obtain considerable energy due to the self-excited vibration characteristics that can cause a quite high amplitude, that is, after a threshold value of flow velocity, the energy harvester can vibrate dramatically and produce a considerable amount of energy [28-31]. Unfortunately, one must consider the issue that it is quite difficult to avoid a galloping or flutter-based energy harvester being damaged due to too large vibratory amplitude if the flow speed cannot be well controlled in a specific region. Fortunately, VIV-based energy harvesting can exactly overcome the aforementioned issue because of the existence of the “lock-in” or “synchronization” phenomenon, that is, when the flow-speed reaches a threshold value, the vortex-induced vibration enters into a resonance-liked stage where the shedding frequency is locked with the natural frequency of the system. Besides, when the flow speed increases beyond the lock-in range, the vibration suppresses immediately. In other words, a VIV-based energy harvester can exactly work as a self-protection system that can adapt the severe weather conditions [32].

Despite large progress on VIV-based energy harvesting, the effect of Reynolds number ($Re = \rho UD/\mu$, ρ is the fluid density, U is the flow velocity, D is the cylinder diameter, μ is the viscosity) on

the performance of a VIV-based energy harvester has seldom been evaluated. It is well-known that the flow regime around a circular cylinder is highly dependent on the Reynolds number. Achenbach and Heinecke [33] identified the laminar, subcritical, and critical flow regimes based on visual observation and changes in Strouhal number (*St*). A more detailed classification of the flow regime around a circular cylinder versus Reynolds number was later proposed by Zdravkovich [34]. Norberg [35] collected experimental measurements of Strouhal number and fluctuating lift coefficient (C_L') in a wide range of Reynolds number, and further proposed empirical formulas to describe the dependence of *St* and C_L' on *Re*, as presented in Fig. 1.

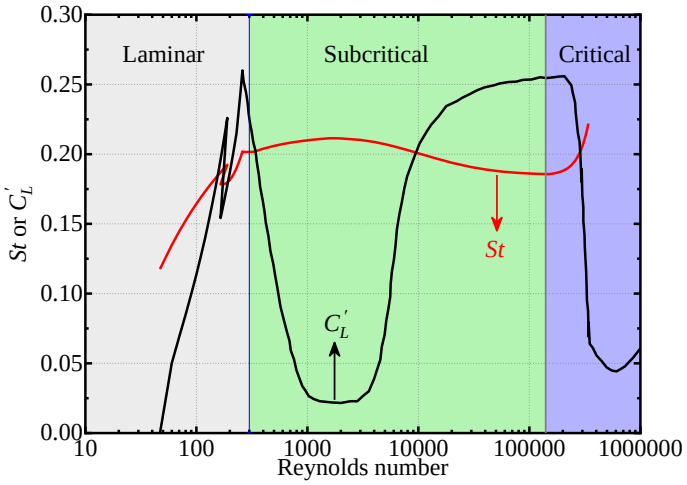

Fig. 1. Strouhal number *St* and fluctuating lift coefficient C_L' in laminar, subcritical, and critical regimes (from Norberg [35]).

Due to the Reynolds number effect on the fluid-elastic effect (e.g., *St*, C_L', and fluid-elastic force), the VIV response of a circular cylinder is also largely affected by the Reynolds number [36-38]. Typical VIV responses of lightly damped circular cylinders in the laminar and subcritical regimes are presented in Fig. 2. The results for *Re* = 4000 originated from the experiments of Govardhan and Williamson [36], while those for *Re* = 90 ~ 150 were obtained from the experiments of Anagnostopoulos and Bearman [39]. It is demonstrated that the Reynolds number affects not only the vibration amplitudes but also the global response behavior. In the subcritical regime, the response consists of three branches, i.e., the initial, upper, and lower branches; however, in the laminar regime, the response only consists of the initial and lower branches. The smaller lock-in range for *Re* = 90 ~ 150 is due to the higher mass-damping parameter and lower Reynolds number. The upper branch in the subcritical regime diminishes with increasing the mass-damping parameter

of the circular cylinder.

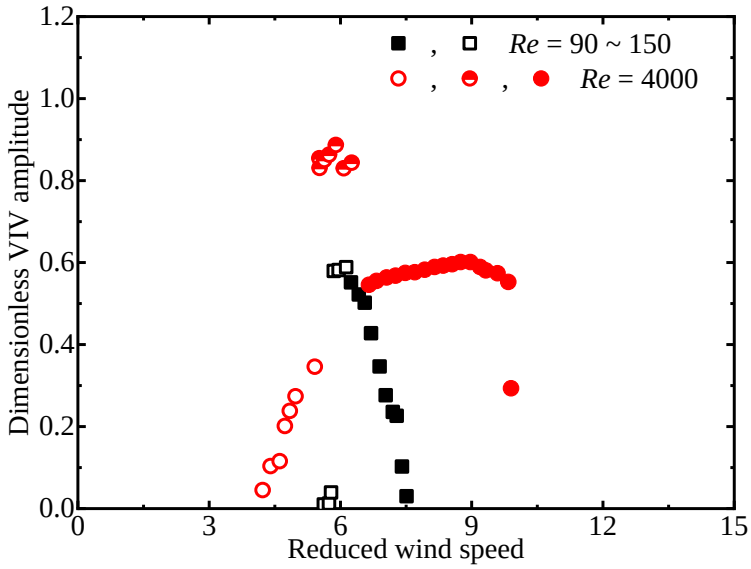

Fig. 2. Dimensionless VIV amplitudes in laminar regime (Re = 90 ~ 150 [39]) and subcritical regime (Re = 4000 [36]); open markers: initial branch; half-open markers: upper branch; solid markers: lower branch.

This paper presents a numerical investigation to study the influence of the Reynolds number on the piezoelectric energy harvesting from vortex-induced vibrations of circular cylinders. A recently-developed aerodynamic damping envelope model [40, 41] is used to simulate the vortex-induced force. The aerodynamic damping envelope model is then implemented into a lumped-parameter model describing the coupled aero-electro-mechanical system of the VIV-based energy harvester. Wind tunnel experiments are conducted to validate the accuracy of the lumped-parameter model and to estimate the power output of the energy harvester. Aerodynamic parameters of the aerodynamic damping envelope model over a Reynolds number range of 500 ~ 33000 are identified based on the modified Griffin plot proposed in [38]. The performance of a VIV-based piezoelectric energy harvester is then evaluated in this Reynolds number range based on the simulated aero-electro-mechanical system.

The subsequent parts of this work are organised as follows. The aerodynamic damping envelope model for VIV and the lumped-parameter model for a VIV-based piezoelectric energy harvester are described in Section 2. The accuracy of the electro-aero-mechanical model is verified by wind tunnel experiments in Section 3. The effect of Reynolds number on the performance of a VIV-based piezoelectric energy harvester is examined in Section 4. The main conclusions are summarized in Section 5.

2. Mathematical modeling of a VIV-based piezoelectric energy harvester

2.1. Aerodynamic damping model for VIV

An elastically-mounted circular cylinder immersed in two-dimensional flow is schematically shown in Fig. 3, in which m denotes the mass per unit span length (including the structural mass and potential fluid added mass), k represents the spring stiffness constant, c is the mechanical damping coefficient, U is the mean wind speed, D is the diameter of the cylinder, F_x and F_y denote the aerodynamic forces in the streamwise and cross-flow directions, respectively. The VIV of a circular cylinder with a relatively large mass ratio (between cylinder and displaced fluid) is often dominated by the vertical (i.e., cross-flow) vibration. The governing equation for the vertical VIV of the circular cylinder can be expressed as [32, 42]:

$$m(\ddot{y} + 2\xi_0\omega_0\dot{y} + \omega_0^2 y) = F_{air}(U_r, \dot{y}, y, Re) \tag{1}$$

where y represents the vertical displacement; the overdot represents the derivative with respect to time t; $\omega_0 = (k/m)^{0.5}$ is the natural frequency of the cylindrical structure; $\xi_0 = c/(2m\omega_0)$ denotes the mechanical damping ratio; $U_r = 2\pi U/\omega_0 D$ is the reduced wind speed; $F_{air} = F_y$ is the aerodynamic force in the cross-flow direction, which is a function of U_r, y, $\dot{y}$ and Re.

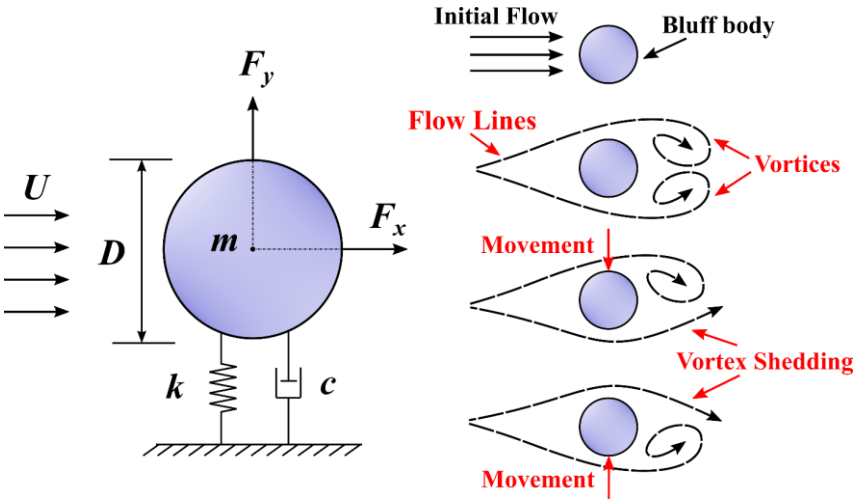

Fig. 3. Schematic diagram of a circular cylinder in two-dimensional flow.

An appropriate expression for the aerodynamic force F_{air} is of great significance to accurately evaluate the VIV response. Several semi-empirical approaches are available for the prediction of VIV, e.g., the two-degree-of-freedom wake oscillator model [43, 44], and the single-degree-of-freedom model [40, 45] in which the aerodynamic force is decomposed into an aerodynamic stiffness component in phase and an aerodynamic damping component in quadrature with the time-varying displacement. A physical sound single-degree-of-freedom modeling scheme is to simulate

the nonlinear aerodynamic force with an amplitude-dependent function of the time-varying displacement and velocity of the cylinder (e.g., [45-48]). Recently, Zhang et al. [42] showed that a model of this type can satisfactorily predict the VIV amplitudes of a circular cylinder in a wide range of mass-damping parameters. Following their model, the aerodynamic force can be expressed as:

$$F_{air} = 0.5\rho U^2 D\left[\frac{2\pi}{U_r}H_1^*(A, U_r, Re)\frac{\dot{y}}{U} + \frac{4\pi^2}{U_r^2}H_4^*(A, U_r, Re)\, y + C_L(U_r, Re)\, sin(\omega_s t + \phi)\right] \quad (2)$$

where ρ is the air density; A represents the amplitude of the non-dimensional displacement y/D; H_1^* and H_4^* are amplitude-dependent aerodynamic damping and stiffness parameters, respectively; C_L is a parameter to characterize the forcing term in the aerodynamic force; $\omega_s = 2\pi S_t U/D$ and ϕ are the shedding frequency and initial phase of the forcing term, respectively.

For lock-in responses with large-amplitude vibrations, the forcing term in the aerodynamic force is negligible [45]. Besides, if the mass ratio between the cylinder and displaced air is large (e.g., of order 10 or 100), the effect of the aerodynamic stiffness term on the VIV response becomes insignificant. As a result, the forcing term and aerodynamic stiffness term can be removed to simplify equation (2):

$$F_{air} = 0.5\rho U^2 D\left[\frac{2\pi}{U_r}\cdot H_1^*(A, U_r, Re)\frac{\dot{y}}{U}\right] \quad (3)$$

The governing equation of the elastically-mounted rigid cylinder, i.e., equation (1), is then formulated as:

$$m(\ddot{y} + 2\xi_0\omega_0\dot{y} + \omega_0^2 y) = 0.5\rho U^2 D\left[\frac{2\pi}{U_r}\cdot H_1^*(A, U_r, Re)\frac{\dot{y}}{U}\right] \quad (4)$$

By moving the left-hand term of equation (4) to the right-hand side, it becomes:

$$\ddot{y} + \frac{2m_a\omega_0}{m}\left[\alpha - \frac{1}{\pi}H_1^*(A, U_r, Re)\right]\dot{y} + \omega_0^2 y = 0 \quad (5)$$

where $\alpha = m\xi_0/m_a$ is a dimensionless mass-damping parameter defined by [49] and $m_a = \pi\rho D^2/4$ is the potential fluid added mass.

As noticed from equation (5), two important parameters that dominate the VIV initiation and amplitude of a circular cylinder are α and $H_1^*(A, U_r, Re)$. Figure 4(a) schematically presents the dimensionless VIV amplitudes for a specific Re at three mass-damping conditions α. The peak VIV amplitudes A_{max} for $\alpha = \alpha_1$, α_2, and α_3 occur at reduced wind speeds of $U_{r,1}$, $U_{r,2}$, and $U_{r,3}$, respectively. The H_1^* curves at $U_{r,1}$, $U_{r,2}$, and $U_{r,3}$ are schematically illustrated in Fig. 4(b).

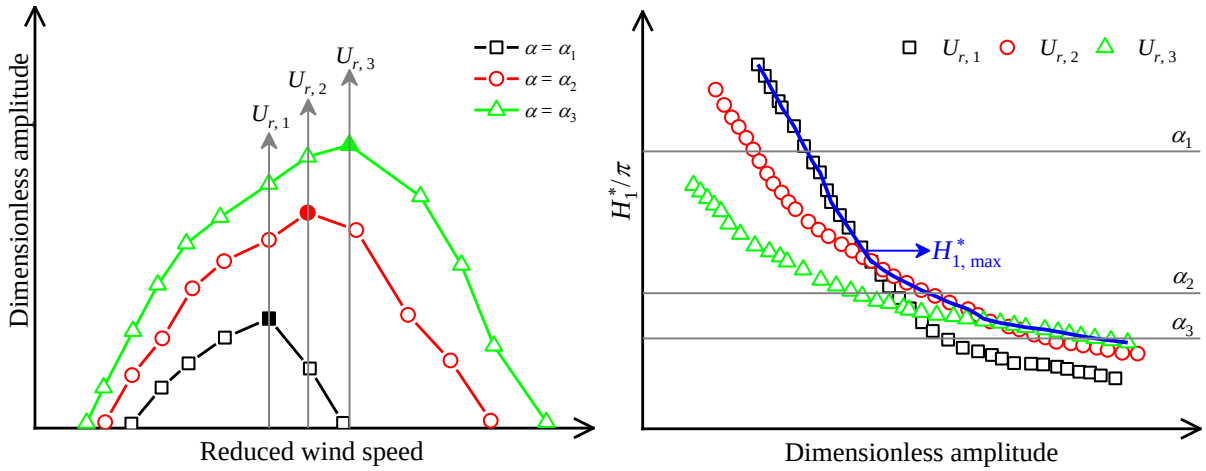

(a) (b)

Fig. 4. Schematic diagrams of (a) dimensionless VIV amplitudes at three mass-damping conditions α and (b) amplitude-dependent aerodynamic damping parameter $H_1^*(A, U_r)$ and aerodynamic damping envelope $H_{1,max}^*(A)$ (blue line) for a specific *Re*. The peak VIV amplitudes A_{max} at three α are highlighted by solid markers in (a).

On the other hand, in order to obtain the maximum power output of a VIV-based energy harvester in the lock-in range, it is beneficial to have a representative model that can directly evaluate the peak VIV amplitude within the lock-in range of a cylinder. For this purpose, the upper envelope of $H_1^*(A, U_r)$ at various reduced flow velocities can be merged into a $H_{1,max}^*(A)$ curve, as highlighted by a blue line in Fig. 4(b). It should be mentioned that the purpose of Fig. 4(b) is to illustrate how to determine $H_{1,max}^*(A)$ based on the $H_1^*(A, U_r)$ schematically. Practically, it is necessary to have the $H_1^*(A, U_r)$ at more reduced flow velocities (i.e., densely distributed in the lock-in range). As the upper boundary of $H_1^*(A, U_r)$, $H_{1,max}^*(A)$ represents the variation of the largest negative aerodynamic damping in the lock-in range versus vibration amplitude.

Zhang et al. [40, 41] showed that equation (6) can be utilized as a simplified aerodynamic force model to conveniently calculate the peak VIV amplitudes A_{max} of a circular cylinder with different mass-damping conditions α:

$$F_{air} = 0.5\rho U^2 D\left[\frac{2\pi}{U_r}\cdot H_{1,max}^*(A, Re)\frac{\dot{y}}{U}\right] \tag{6}$$

Equation (6) is referred to as the aerodynamic damping envelope model by Zhang et al. [40], and $H_{1,max}^*(A)$ is the aerodynamic damping envelope. The following equation can be employed to calculate the peak VIV amplitudes in the lock-in range of a circular cylinder at various α and *Re*.

$$m(\ddot{y} + 2\xi_0\omega_0\dot{y} + \omega_0^2 y) = 0.5\rho U^2 D\left[\frac{2\pi}{U_r}\cdot H_{1,max}^*(A, Re)\frac{\dot{y}}{U}\right] \tag{7}$$

It should be highlighted that the aerodynamic parameter $H_1^*(A, U_r, Re)$ in the model of

equation (3) is a function of the reduced flow velocity, and hence the model can be utilized to predict the VIV amplitudes at various reduced flow velocities in the entire lock-in range. On the other hand, the aerodynamic parameter $H_{1,max}^{*}(A, Re)$ in the model of equation (6) is independent of the reduced flow velocity since the model is developed to conveniently evaluate the peak VIV amplitude without calculating the VIV amplitudes in the entire lock-in range.

As discussed by Zhang et al. [41], $H_1^{*}(A, U_r)$ for a specific *Re* can be extracted according to the VIV displacement signals (grow-to-resonance and/or decay-to-resonance) at a single mass-damping parameter α. For a specific *Re*, once $H_1^{*}(A, U_r)$ are available in the interested ranges of *A* and U_r, $H_{1,max}^{*}(A)$ could be then obtained through the least square fitting based on the upper boundary of $H_1^{*}(A, U_r)$, as illustrated in Fig. 4(b). However, to identify the aerodynamic parameters at different *Re* by this method, a huge amount of experimental work is required to obtain the experimental VIV signals at various *Re*.

A more practical method is to identify $H_{1,max}^{*}(A, Re)$ based on the Griffin plot (i.e., peak VIV amplitude A_{max} versus mass-damping parameter α) at various *Re*. At the peak VIV amplitude, the energy absorbed from flow is completely dissipated by mechanical damping. Hence, the equivalent negative aerodynamic damping ratio is equal to the mechanical damping ratio. Accordingly, for a specific α and *Re*, $H_{1,max}^{*}$ at the peak VIV amplitude can be obtained according to equation (7) as:

$$H_{1,max}^{*}(A_{max}) = \pi\alpha \tag{8}$$

Govardhan and Williamson [36] systematically collected the experimental VIV steady-state amplitudes reported before 2006. They showed that, over the range of *Re* = 500 ~ 33000, the peak VIV amplitudes A_{max} can be approximated as:

$$\begin{aligned} A_{max} &= (1 - 1.12\alpha + 0.30\alpha^2)\, log(\,0.41\, Re^{0.36}) \\ &= (1 - 1.12\frac{H_{1,max}^{*}}{\pi} + 0.30\frac{(H_{1,max}^{*})^2}{\pi^2})\, log(\,0.41\, Re^{0.36}) = g\left(H_{1,max}^{*}, Re\right) \end{aligned} \tag{9}$$

According to equation (9), $H_{1,max}^{*}$ can be approximated as:

$$H_{1,max}^{*} = g^{-1}(A_{max}, Re) \tag{10}$$

For each specific *Re*, an amplitude-dependent $H_{1,max}^{*}$ function can be obtained from equations (9) and (10). It should be noted that the applicability of equation (10) should be limited within *Re* = 500 ~ 33000. Fortunately, this covers the interested *Re* range for a lot of practical VIV-based

energy piezoelectric harvesters. The only purpose of introducing equations (8) ~ (10) is to identify the $H^*_{1,max}(A)$ curves at various Re. The identified $H^*_{1,max}(A)$ curves can be used as input aerodynamic parameters to calculate the displacement responses and output power values of an energy harvester at various Re and α.

To check the validity of the $H^*_{1,max}$ calculated by equation (10), the peak VIV amplitudes of an elastically-mounted circular cylinder are predicted by the aerodynamic model at Re = 4000 and 12000, as presented in Fig. 5 together with available experimental measurements by Govardhan and Williamson [36]. It is noted that the predicted peak VIV amplitudes agree very well with the experimental measurements, suggesting that the $H^*_{1,max}$ can be accurately calculated from equation (10).

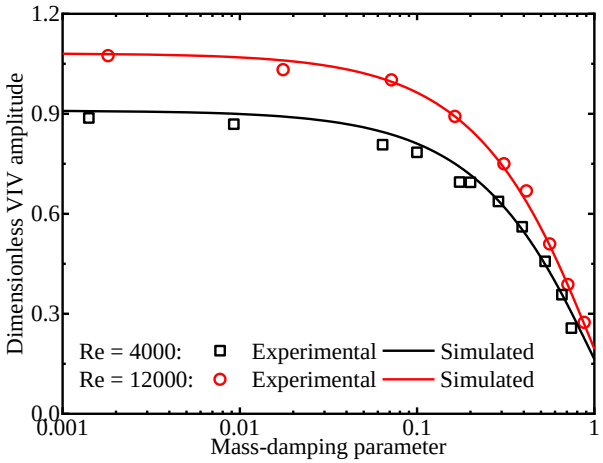

Fig. 5. Verification of $H^*_{1,max}$ calculated by equation (10): comparison of experimental [36] and predicted peak VIV amplitudes.

2.2. Estimation of the harvested power

As shown in Fig. 6, a typical VIV-based piezoelectric energy harvester consists of a circular cylinder, a cantilever beam, and a piezoelectric transducer bonded at the root of the beam. Vibration of the beam can be excited by the aerodynamic force acting on the circular cylinder, which leads to power generation by the piezoelectric transducer. The lumped-parameter model for the aero-electro-mechanical system can be expressed as [22, 23, 50]:

$$m(\ddot{y} + 2\xi_0\omega_0\dot{y} + \omega_0^2 y) + \theta V(t) = F_{air}(t) \tag{11a}$$

$$I(t) + C_p\dot{V}(t) - \theta\dot{y}(t) = 0 \tag{11b}$$

where m is the equivalent mass of the VIV-based piezoelectric energy harvester, y denotes the transverse displacement of the circular cylinder, V is the generated voltage, C_p is the capacitance

measured experimentally, $I = V/R$ represents the current flowing into the interface circuit, R is the electrical load resistance, θ represents the electromechanical coupling coefficient.

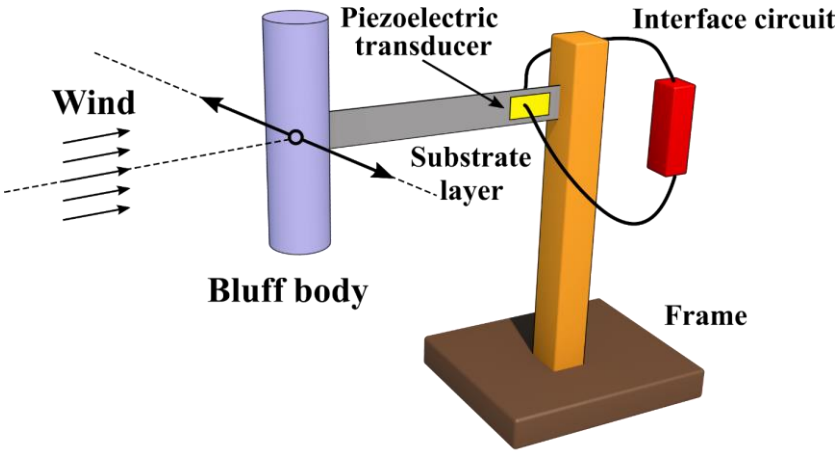

Fig. 6. Schematic implementation of a VIV-based piezoelectric energy harvester.

Substituting equation (3) into equation (11a), the resulting equation (12) can be utilized together with equation (11b) to calculate the VIV responses and power outputs in the entire lock-in range:

$$m(\ddot{y} + 2\xi_0\omega_0\dot{y} + \omega_0^2 y) + \theta V(t) = 0.5\rho U^2 D\left[\frac{2\pi}{U_r}\cdot H_1^*(A, U_r, Re)\frac{\dot{y}}{U}\right] \quad (12)$$

Substituting equation (6) into equation (11a), the resulting equation (13) can be utilized together with equation (11b) to obtain the peak VIV amplitude and peak power output in the lock-in range:

$$m(\ddot{y} + 2\xi_0\omega_0\dot{y} + \omega_0^2 y) + \theta V(t) = 0.5\rho U^2 D\left[\frac{2\pi}{U_r}\cdot H_{1,max}^*(A, Re)\frac{\dot{y}}{U}\right] \quad (13)$$

3. Validation of equivalent electro-aero-mechanical model

3.1. Wind tunnel experiments

Wind tunnel experiments are carried out to determine the accuracy of the electro-aero-mechanical model for the VIV-based piezoelectric energy harvester developed in Section 2. A wind tunnel with round cross-section (diameter = 0.40 m) is utilized to test the performance of a VIV-based piezoelectric energy harvester. As presented in Fig. 7(a), the wind tunnel can generate stable incoming flow by installing a honeycomb structure inside the settling chamber, as shown in Fig. 7(c). The wind speed is adjustable in the range of $0 \leqslant U \leqslant 7$ m/s, and the freestream turbulent intensity is measured to be lower than 0.5%. A piezoelectric patch (PZT-5, Jiayeshi.co., China) of $37 \times 11 \times 0.6$ mm^3 is bonded on a substrate made of pure aluminium in a dimension of $200 \times 25 \times 0.5$ mm^3 to form the piezoelectric cantilever beam. The capacitance of the piezoelectric transducer C_p is 26.0 nF. A circular cylinder is connected at the free end of a piezoelectric cantilever beam, as shown in Fig. 7(b). The circular cylinder is a 0.118 m-long hard foam with a diameter of 0.032 m.

The mechanical damping ratio ξ_0 of the piezoelectric harvester can be calculated according to the free vibration decay response in still air using the logarithmic decrement technique. A hot-wire anemometer (Model: 405i, Testo Co, USA) is adopted to measure the wind velocity U. The voltage output of the harvester is measured by a digital oscilloscope (Model: DS1104S, RIGOL, China). Main parameters of the prototype in the present experiments are listed in Table 1. The Reynolds number range of the present experiments is Re = 4000 ~ 6000, and the peak VIV amplitude occurs at $Re \approx 5000$.

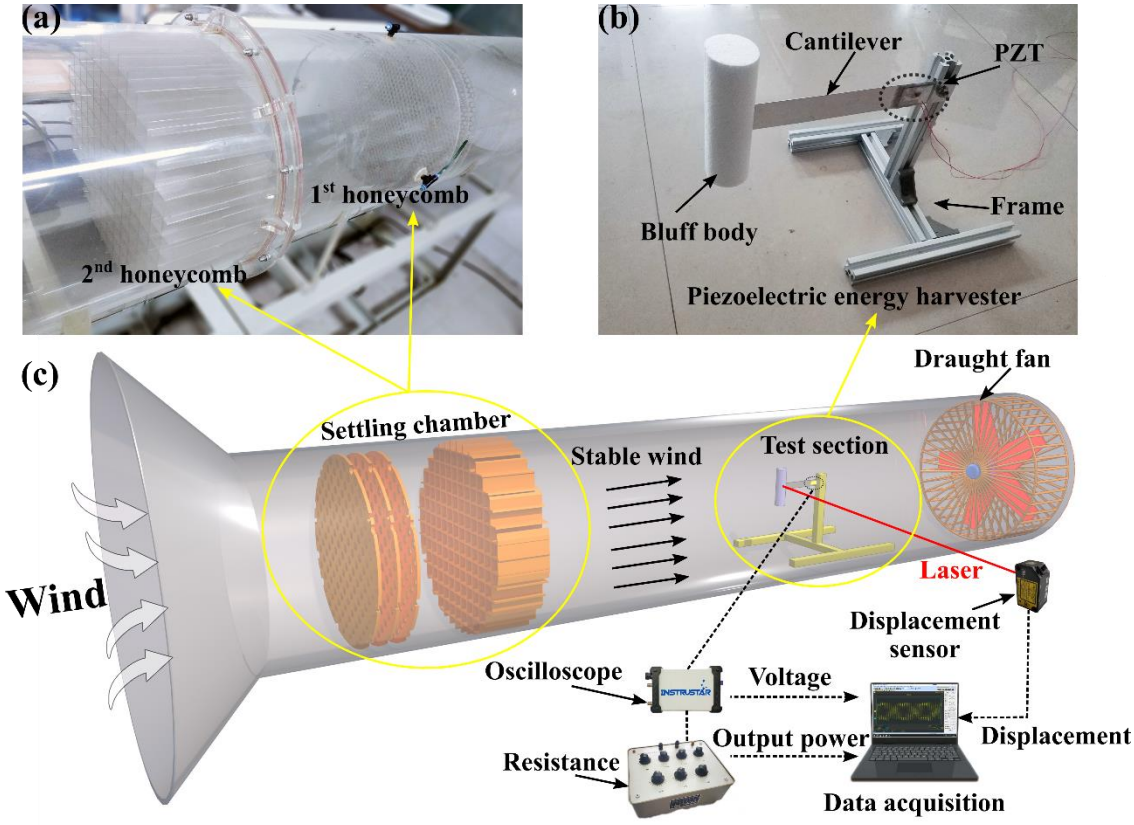

Fig. 7. Experiments setup: (a) wind tunnel; (b) VIV-based piezoelectric energy harvester; (c) the settling chamber.

Table 1. Parameters of VIV-based piezoelectric energy harvester.

Property	Value
Equivalent mass m (g)	3.5
Mechanical damping ratio ξ_0	0.010
Natural frequency ω_0 (rad/s)	55.79
Capacitance C_p (nF)	26
Electromechanical coupling coefficient θ (N/V)	6.6e-6

To identify the aerodynamic parameters H_1^*, the VIV grow-to-resonance signals are recorded at various wind speeds. Some examples are presented in Fig. 8. For a specific reduced flow velocity U_r, the amplitude-dependent damping ratio $\xi(A/D)$ of a grow-to-resonance displacement signal can be identified with the algorithm developed by Zhang and Xu [51]. The equivalent aerodynamic damping ratio can be expressed as:

$$\xi_{aero}(A/D) = \xi(A/D) - \xi_0 \tag{14}$$

H_1^* at this reduced wind speed is then obtained as:

$$H_1^* = \frac{4m\xi_{aero}(A/D)}{\rho D^2} \tag{15}$$

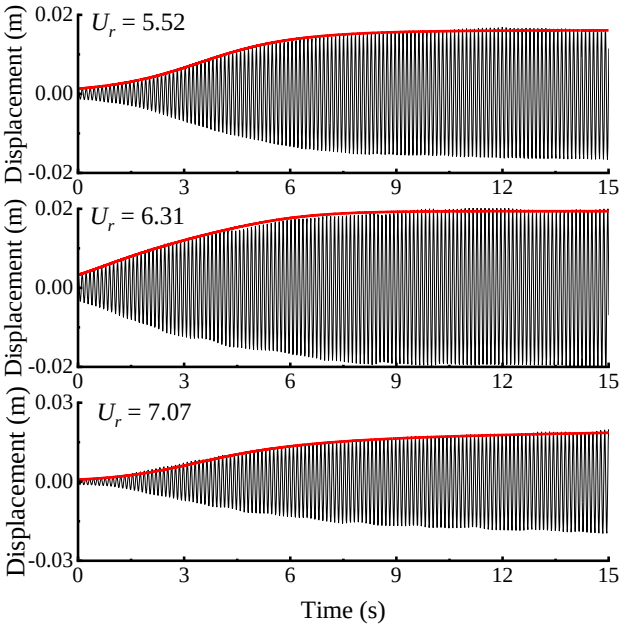

Fig. 8. VIV responses of a VIV-based piezoelectric energy harvester. black line: experimental displacement history; red line: time-varying amplitude of simulated displacement history.

H_1^* for various U_r are identified based on the grow-to-resonance signals, as presented in Fig. 9. The identified H_1^* can be used as input aerodynamic parameters for equation (12) to calculate the displacement responses and output power values of the VIV-based piezoelectric energy harvester at various reduced wind speeds.

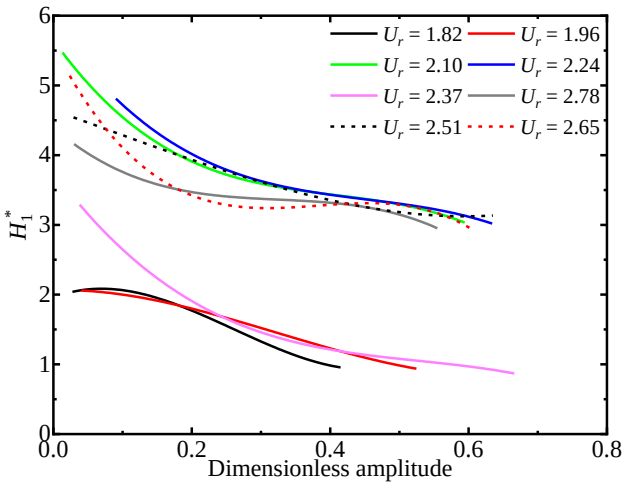

Fig. 9. Experimentally identified H_1^* of a VIV-based piezoelectric energy harvester.

3.2. Comparison between experimental and simulated results

The plotted curves in Fig. 8 compare the experimental and simulated VIV displacement time-histories to verify the aerodynamic force model described in Section 2.1. Results of three reduced wind speeds, i.e., near the onset threshold, in the middle of the lock-in range, and near the end threshold, are presented. It is noted that the time-varying amplitudes of simulated displacement histories agree very well with the experimental results, for both amplitude-increasing stage and steady-state stage.

To validate the representative model for the aero-electro-mechanical system described in Section 2.2, the experimental and simulated VIV amplitudes and power outputs of the piezoelectric energy harvester are compared. Figure 10 compares the experimentally measured and simulated power outputs versus load resistance at a reduced wind speed of U_r = 5.91. The prediction error is smaller than 5% for most load resistances, while the error is higher than 15% for R = 100, 3000 and 50000 kΩ. This should be mainly due the errors of the identified aerodynamic, mechanical, and electrical parameters. Figure 11 compares the experimentally measured and simulated VIV amplitudes and power outputs versus the reduced wind speed in the lock-in range. The average power is calculated using Joule's law in conjunction with Ohm's law: average power = RMS voltage × RMS voltage/load resistance (RMS: root mean square). It is noted that the simulated results agree quite well with the experimental measurements. Indeed, both the optimal load resistance and power outputs in the lock-in range can be satisfactorily produced by the representative electro-aero-mechanical model. The comparisons confirm that this model can be utilized to simulate the behavior of the VIV-based piezoelectric energy harvester with reasonable accuracy. Hence, the

representative electro-aero-mechanical model of equation (12) can be utilized to study the effect of Reynolds number on the performance of VIV-based piezoelectric energy harvesters.

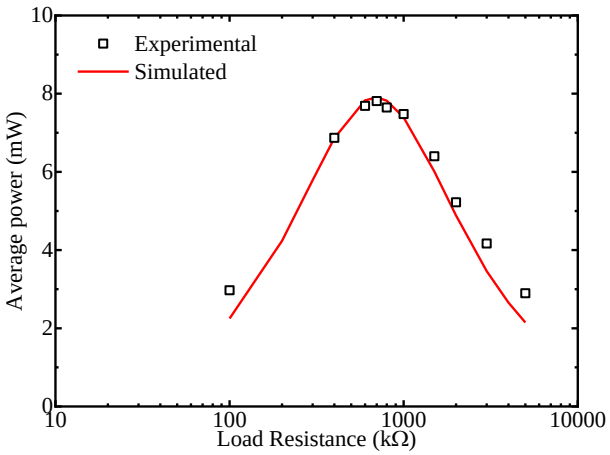

Fig. 10. Validation of the representative electro-aero-mechanical model: average power versus load resistance.

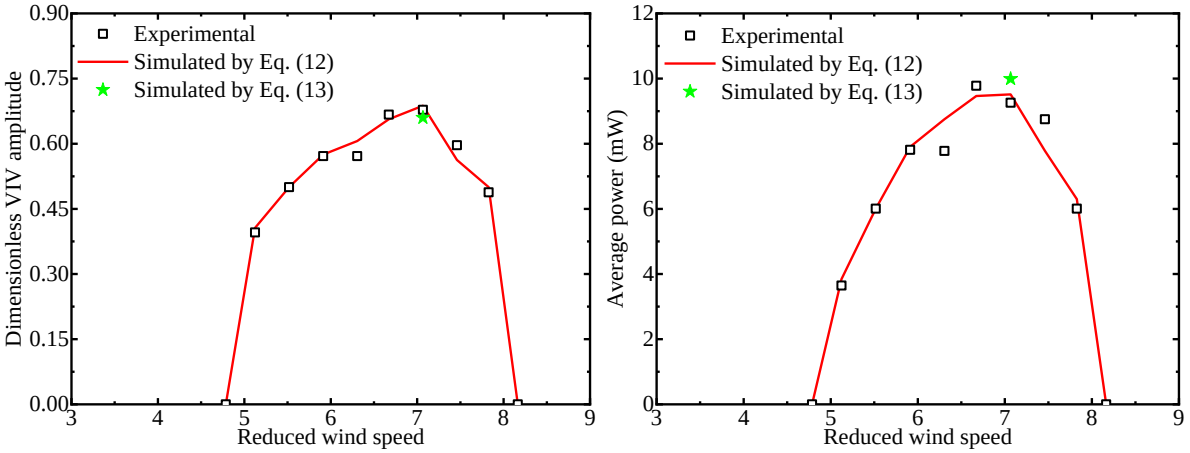

Fig. 11. Comparative bifurcation diagrams between experimental measurements and developed model: (a) dimensionless VIV amplitude versus reduced wind speed and (b) average power versus reduced wind speed. Red line: results simulated by equation (12) with experimentally identified H_1^*; green star: results simulated by equation (13) with $H_{1,max}^*$ calculated based on equation (10).

As stated earlier, the maximum VIV amplitude (and hence the maximum power output) of the present experiments occurs at $Re \approx 5000$. $H_{1,max}^*$ for $Re = 5000$ is calculated based on equation (10) and then substituted into equation (13) to calculate the maximum VIV amplitude and maximum power output. As presented in Fig. 11, the resulting maximum dimensionless amplitude and maximum power output are 0.66 and 9.99 mW, respectively, which agree well with the experimental values (0.69 and 9.51 mW, respectively). The agreements suggest that equation (10) can be used to calculate the aerodynamic damping envelope, and hence equation (13) is applicable to calculate the maximum VIV amplitude and maximum power output of a VIV-based piezoelectric

energy harvester at various Reynolds numbers.

4. Effect of *Re* on performance of a VIV-based piezoelectric energy harvester

4.1. Effect of *Re* on power output in the lock-in range

In order to demonstrate the Reynolds number effect on the levels of the harvested power of a VIV-based piezoelectric energy harvester in the lock-in range, the power outputs at three typical Reynolds numbers, i.e., Re = 100 in the laminar regime, and Re = 4000 ~ 6000 and Re = 10000 in the subcritical regime will be calculated based on the representative electro-aero-mechanical model of equation (12). The aerodynamic damping parameters H_1^* for Re = 4000 ~ 6000 are identified from the experiments in Section 3, as presented in Fig. 9. The H_1^* for Re = 10000 are constructed from the forced vibration experiments of [52], as shown in Fig. 12(a).

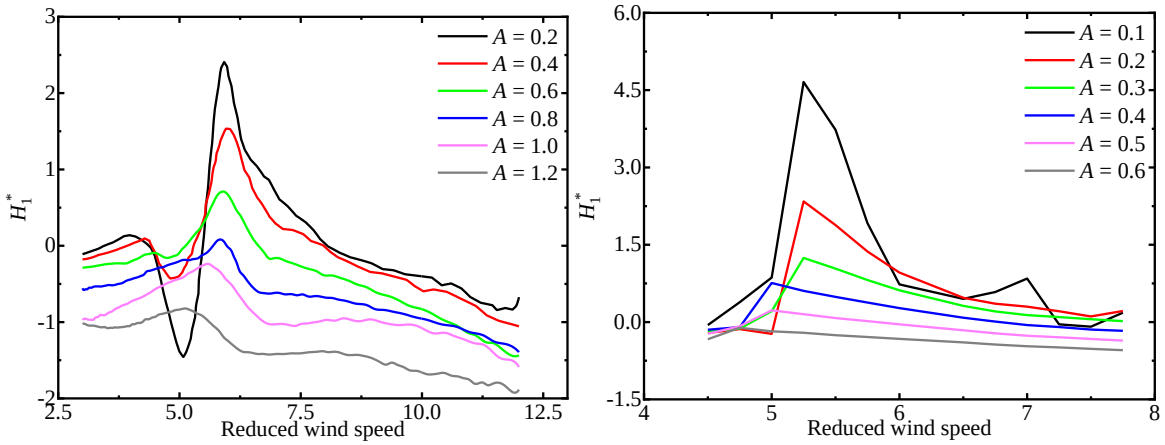

(a) (b)

Fig. 12. H_1^* of a circular cylinder: (a) Re = 10000 and (b) Re = 100.

The H_1^* for Re = 100 are identified based on the computational simulation procedure developed in [47, 48]. Forced vibration numerical simulations (two-dimensional unsteady Reynolds-Averaged Navier–Stokes simulations) are conducted based on the commercial program ANSYS FLUENT. The computational domain and boundary conditions are schematically shown in Fig. 13(a). The computational domain extends upstream and downstream the circular cylinder by 10d. Around the circular cylinder, refined quadrilateral cells are generated with an initial thickness of 0.03 mm at the tube surface and a growth factor of 1.15 along the radial direction until the 20th layer. Unstructured grids are used for the rest of the computational domain. The total grid number is 45626, which is proved to be enough according to a sensitivity study of mesh dependency. Figure 13(b) presents a partial view of the mesh around the tube surfaces. The time step length is selected according to a sensitivity study, which proves that a time step of 0.005 s is sufficient to ensure the

simulation. The simulated H_1^* are given in Fig. 12(b).

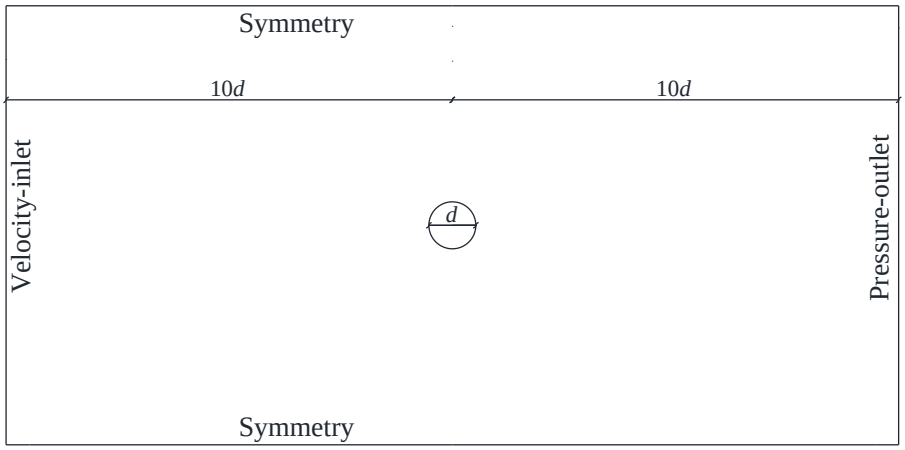

(a)

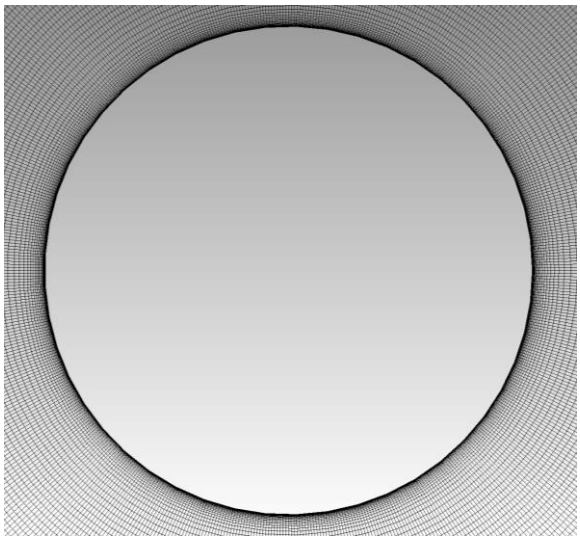

(b)

Fig. 13. Numerical simulation of a circular cylinder: (a) computational domain and boundary conditions and (b) mesh details around the circular cylinder.

The aerodynamic parameters H_1^* for Re = 100, Re = 4000 ~ 6000, and Re = 10000 are substituted into the representative electro-aero-mechanical model of equation (12) to calculate the displacement responses and power outputs of the VIV-based piezoelectric energy harvester in the lock-in range. The mass, damping, and electrical parameters for the VIV-based piezoelectric energy harvester are the same as those given in Table 1. The performances of the VIV-based piezoelectric energy harvester at three different Reynolds numbers are given in Fig. 14. It is noted that the Reynolds number affects not only the values, but also the global branches of the power output. The maximum power output at Re = 100 is about 6.62 mW, while that at Re = 4000 ~ 6000 and Re = 12000 are about 9.51 and 14.4 mW, respectively. The effective wind range for power harvesting is also affected by the Reynolds number. Similar to the VIV responses for Re = 90 ~ 150 given in Fig.

1, the results for *Re* = 100 in the laminar regime consists of an initial branch and a lower branch. The results in the subcritical regime are supposed to include three branches, i.e., the initial, upper, and lower branches. The upper branches are not clear for the two cases (*Re* = 4000 ~ 6000 and *Re* = 10000) due to the limited available reduced wind speeds. However, according to [36], the results with dimensionless amplitude higher than 0.6 belong to the upper branch. Therefore, the results for *Re* = 4000 ~ 6000 and *Re* = 10000 both include three branches. These observations highlight the necessity to consider the Reynolds number effect in the design of a VIV-based piezoelectric energy harvester. For a specific VIV-based piezoelectric energy harvester, several measures (e.g., increasing the surface roughness, the diameter, and the natural frequency) could be adopted to increase its working Reynolds number range.

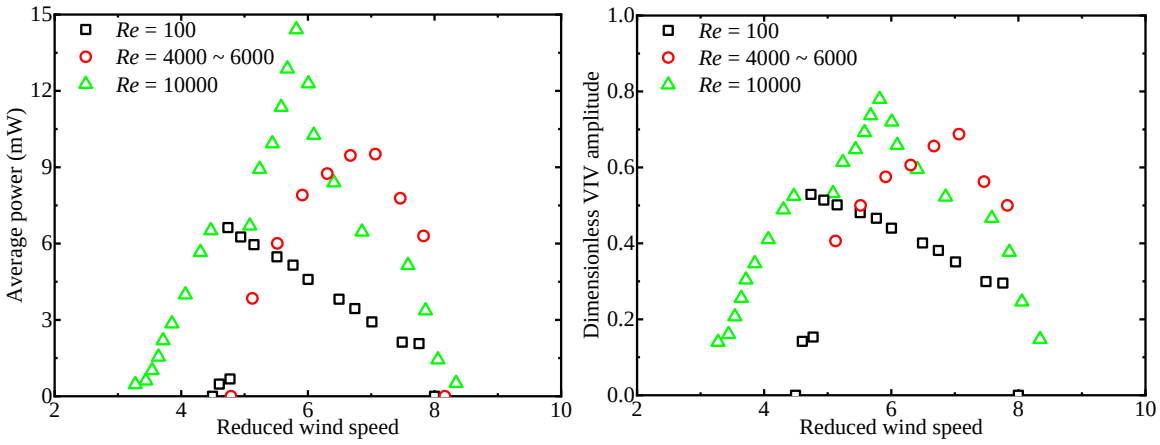

(a) (b)

Fig. 14. Performances of a VIV-based piezoelectric energy harvester at three different Reynolds numbers: (a) dimensionless VIV amplitude versus reduced wind speed and (b) average power versus reduced wind speed.

Figure 15 presents the performances of the VIV-based piezoelectric energy harvester at various load resistances *R* for *Re* = 4000 ~ 6000 and *Re* = 10000. The results of the VIV amplitudes are not shown since they are only slightly affected by the load resistance. It is noted that the optimal load resistance is not affected by the reduced wind speed because it depends on the capacitance and natural frequency of the system which are considered constant in this study. The lock-in range is insignificantly affected by the load resistance in the considered range, which agrees with the observations in Wang et al. [50].

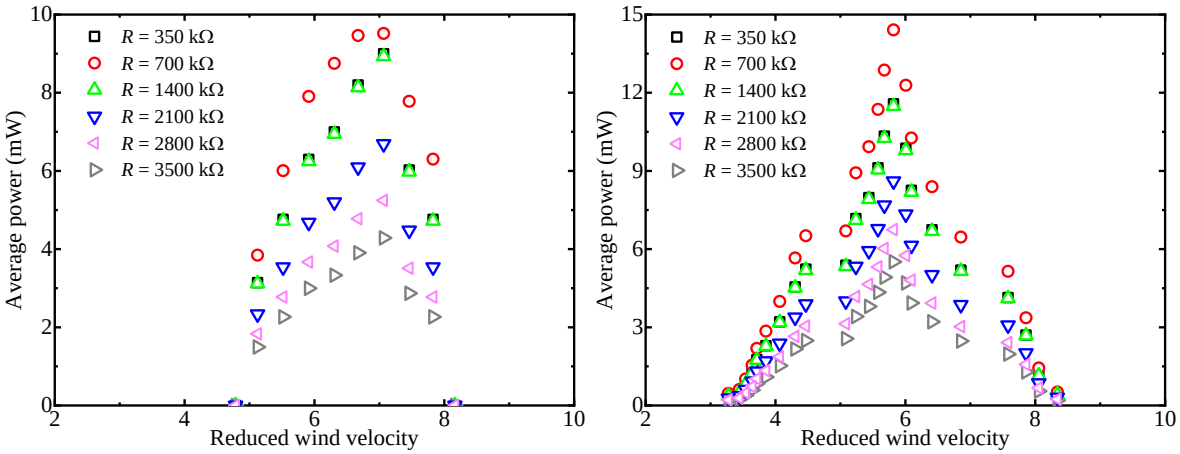

Fig. 15. Performances of a VIV-based piezoelectric energy harvester at various load resistances: (a) *Re* = 4000 ~ 6000 and (b) *Re* = 10000.

4.2. Effect of *Re* on maximum power output

After highlighting the effect of Reynolds number on the performance of a VIV-based piezoelectric energy harvester in Section 4.1, the effect of Reynolds number on the maximum harvested power output is examined in this section. The representative electro-aero-mechanical model of equation (13) can be utilized together with the aerodynamic damping envelope $H_{1,max}^{*}$ calculated by equation (10) to study the Reynolds number effect on the maximum harvested power output for a VIV-based piezoelectric energy harvester. Figure 16 presents the variation of maximum power output as a function of the electrical load resistance at various Reynolds numbers. The mass and electrical parameters for the VIV-based piezoelectric energy harvester are the same as those given in Table 1, while a zero mechanical damping is adopted to obtain the highest VIV amplitudes and power outputs at various *Re*. The maximum power output increases with the load resistance until an optimal value, and then decreases. The optimal load resistance is not affected by the Reynolds number because it depends on the capacitance and natural frequency of the system which are considered constant in this study. The effect of the Reynolds number on the maximum power output is also clearly highlighted in Fig. 16. The maximum power output increases with increasing the Reynolds number. The value at *Re* =500 is about 7.9 mW, while that at *Re* = 30000 is as high as 34.5 mW.

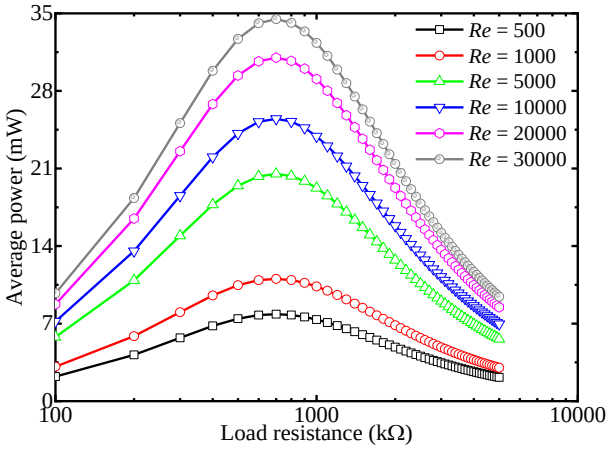

Fig. 16. Variation of maximum power output versus load resistance at various Reynolds numbers.

The variation of maximum power output versus Reynolds number is shown in Fig. 17 for several mechanical damping levels. It is noted that the maximum power output decreases with increasing the mechanical damping ratio ξ_0. For Re = 30000, the maximum power output at ξ_0 = 3.0% is 1.7 mW, while that at ξ_0 = 0 is as high as 34.5 mW. For lower mechanical damping ratio, the maximum power output varies significantly with the Reynolds number. However, the Reynolds number effect is significantly reduced by increasing the mechanical damping ratio. For ξ_0 = 0, the maximum power output increases from 7.9 mW to 35.3 mW as the Reynolds number increase from 500 to 33000. As a comparison, for ξ_0 = 3.0%, the maximum power output increases from 0.39 mW to 1.56 mW as the Reynolds number increase from 500 to 33000. The results indicate that the performance of a VIV-based piezoelectric energy harvester is more sensitive to the Reynolds number for a case with low mechanical damping ratio.

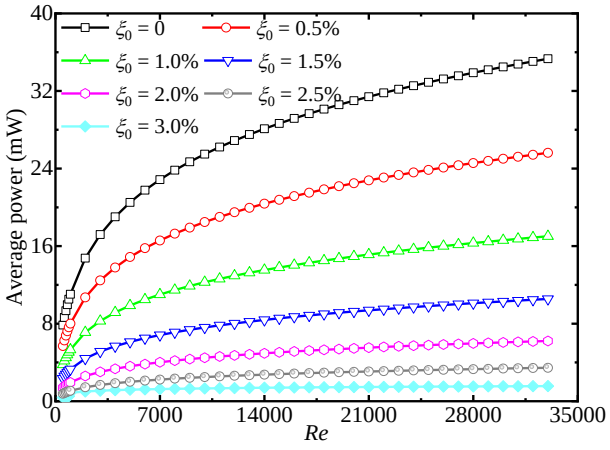

Fig. 17. Variation of maximum power output versus Reynolds number at various mechanical damping levels.

The variation of maximum power output versus mechanical damping ratio is shown in Fig. 18 for several Reynolds numbers. It is noted that the effect of mechanical damping ratio on the

maximum power output is more profound for higher Reynold numbers. For *Re* = 30000, the maximum power output decreases from 34.5 mW to 1.7 mW as the mechanical damping ratio increases from 0 to 3.0%. For *Re* = 500, the maximum power output decreases from 3.3 mW to 0.7 mW as the mechanical damping ratio increases from 0 to 3.0%. The results suggest that the performance of a VIV-based piezoelectric energy harvester is more sensitive to the mechanical damping at high Reynolds number.

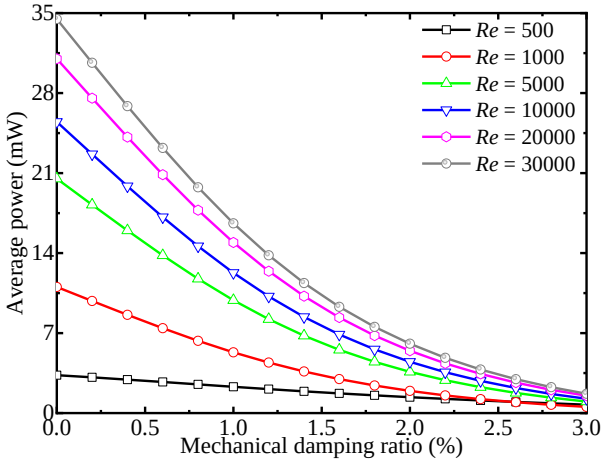

Fig. 18. Variation of maximum power output versus mechanical damping ratio at various Reynolds numbers.

5. Conclusions

This paper presented a numerical investigation to study the effect of Reynolds number on piezoelectric energy harvesting from vortex-induced vibration of a circular cylinder. The aerodynamic force was simulated by a model with amplitude-dependent aerodynamic parameters and an aerodynamic damping envelope model. The amplitude-dependent aerodynamic parameters at two typical Reynolds numbers were identified based on free vibration experiments and forced vibration numerical simulations, respectively. The aerodynamic damping envelopes over a Reynolds number range of 500 ~ 33000 were identified based on the Reynolds number-dependent Griffin plot (a plot showing the peak VIV amplitude versus the mass-damping parameter) proposed by Govardhan and Williamson [36]. The mechanical parameters and piezoelectric coupling in the system were represented by the standard electronic components. The aerodynamic, mechanical, and piezoelectric blocks were implemented into a representative electro-aero-mechanical model to simulate the aero-electro-mechanical system of the VIV-based piezoelectric energy harvester. Wind tunnel experiments were carried out to validate the accuracy of the representative electro-aero-

mechanical model for the VIV-based piezoelectric energy harvester. A parametric study was then presented to study the Reynolds number effect on the bifurcation diagrams and maximum power output of a VIV-based piezoelectric energy harvester. Some important conclusions were given as:

(1) Both the lock-in range and power outputs within lock-in of a VIV-based piezoelectric energy harvester increase with increasing the Reynolds number. The Reynolds number also affects the global branches of the power output: in the subcritical regime, the power output consists of three branches, i.e., initial, upper, and lower branches; however, in the laminar regime, the power output only consists of the initial and lower branches. The upper branch in the subcritical regime diminished with increasing the mass-damping parameter.

(2) The optimal load resistance of a VIV-based piezoelectric energy harvester was almost not affected by the Reynolds number when the same capacitance and natural frequency are considered. The performance of an energy harvester is more sensitive to the Reynolds number for a case with a low mechanical damping ratio. On the other hand, the performance of an energy harvester is more sensitive to mechanical damping at a high Reynolds number.

Acknowledgments

This work was supported by the National Natural Science Foundation of China (Grant No.: 51977196), and China Postdoctoral Science Foundation (2020T130557).

References

1. Prauzek, M., Konecny, J., Borova, M., Janosova, K., Hlavica, J., Musilek, P., *Energy harvesting sources, storage devices and system topologies for environmental wireless sensor networks: A review.* Sensors, 2018. **18**(8): p. 2446.
2. Yang, Z., Zhou, S., Zu, J., Inman, D., *High-performance piezoelectric energy harvesters and their applications.* Joule, 2018. **2**(4): p. 642-697.
3. Abdelkefi, A., *Aeroelastic energy harvesting: A review.* International Journal of Engineering Science, 2016. **100**: p. 112-135.
4. Chen, Z., Xia, Y., He, J., Xiong, Y., Wang, G., *Elastic-electro-mechanical modeling and analysis of piezoelectric metamaterial plate with a self-powered synchronized charge extraction circuit for vibration energy harvesting.* Mechanical Systems and Signal Processing, 2020. **143**: p. 106824.
5. Gu, Y., Liu, W., Zhao, C., Wang, P., *A goblet-like non-linear electromagnetic generator for planar multi-directional vibration energy harvesting.* Applied Energy, 2020. **266**: p. 114846.
6. Wu, Y., Qiu, J., Zhou, S., Ji, H., Chen, Y., Li, S., *A piezoelectric spring pendulum oscillator used for multi-directional and ultra-low frequency vibration energy harvesting.* Applied energy, 2018. **231**: p. 600-614.

7. Fan, K., Cai, M., Liu, H., Zhang, Y., *Capturing energy from ultra-low frequency vibrations and human motion through a monostable electromagnetic energy harvester.* Energy, 2019. **169**: p. 356-368.
8. Lai, Z., Wang, J., Zhang, C., Zhang, G., Yurchenko, D., *Harvest wind energy from a vibro-impact DEG embedded into a bluff body.* Energy Conversion and Management, 2019. **199**: p. 111993.
9. Yang, Z., Tang, L., Yu, L., Tao, K., Aw, K., *Modelling and analysis of an out-of-plane electret-based vibration energy harvester with AC and DC circuits.* Mechanical Systems and Signal Processing, 2020. **140**: p. 106660.
10. Tao, K., Yi, H., Yang, Y., Chang, H., Wu, J., Tang, L., Yang, Z., Wang, N., Hu, L., Fu, Y., *Origami-inspired electret-based triboelectric generator for biomechanical and ocean wave energy harvesting.* Nano Energy, 2019: p. 104197.
11. Lai, Z., Wang, S., Zhu, L., Zhang, G., Wang, J., Yang, K., Yurchenko, D., *A hybrid piezo-dielectric wind energy harvester for high-performance vortex-induced vibration energy harvesting.* Mechanical Systems and Signal Processing, 2021. **150**: p. 107212.
12. Liu, H., Fu, H., Sun, L., Lee, C., Yeatman, E.M., *Hybrid energy harvesting technology: From materials, structural design, system integration to applications.* Renewable and Sustainable Energy Reviews, 2020: p. 110473.
13. Song, D., Fan, X., Yang, J., Liu, A., Chen, S., Joo, Y.H., *Power extraction efficiency optimization of horizontal-axis wind turbines through optimizing control parameters of yaw control systems using an intelligent method.* Applied energy, 2018. **224**: p. 267-279.
14. Song, D., Zheng, S., Yang, S., Yang, J., Dong, M., Su, M., Joo, Y.H., *Annual Energy Production Estimation for Variable-Speed Wind Turbine at High-Altitude Site.* Journal of Modern Power Systems and Clean Energy, 2020.
15. Zhao, L.-C., Zou, H.-X., Yan, G., Liu, F.-R., Tan, T., Zhang, W.-M., Peng, Z.-K., Meng, G., *A water-proof magnetically coupled piezoelectric-electromagnetic hybrid wind energy harvester.* Applied Energy, 2019. **239**: p. 735-746.
16. Qin, C., Innes-Wimsatt, E., Loth, E., *Hydraulic-electric hybrid wind turbines: Tower mass saving and energy storage capacity.* Renewable Energy, 2016. **99**: p. 69-79.
17. Rus, T., Rus, L.F., Abrudan, A.C., Domnita, F.V., Mare, R., *Experimental tests in equipping vertical axis wind turbines with electric Generator.* International Journal of Renewable Energy Research (IJRER), 2016. **6**(2): p. 465-471.
18. Wang, D.-A., Ko, H.-H., *Piezoelectric energy harvesting from flow-induced vibration.* Journal of Micromechanics and Microengineering, 2010. **20**(2): p. 025019.
19. Wang, J., Geng, L., Ding, L., Zhu, H., Yurchenko, D., *The state-of-the-art review on energy harvesting from flow-induced vibrations.* Applied Energy, 2020. **267**: p. 114902.
20. Zhu, H., Zhao, Y., Zhou, T., *CFD analysis of energy harvesting from flow induced vibration of a circular cylinder with an attached free-to-rotate pentagram impeller.* Applied energy, 2018. **212**: p. 304-321.
21. Ding, L., Mao, X., Yang, L., Yan, B., Wang, J., Zhang, L., *Effects of installation position of fin-shaped rods on wind-induced vibration and energy harvesting of aeroelastic energy converter.* Smart Materials and Structures, 2021. **30**(2): p. 025026.
22. Mehmood, A., Abdelkefi, A., Hajj, M., Nayfeh, A., Akhtar, I., Nuhait, A., *Piezoelectric energy harvesting from vortex-induced vibrations of circular cylinder.* Journal of Sound and Vibration, 2013. **332**(19): p. 4656-4667.
23. Wang, J., Gu, S., Zhang, C., Hu, G., Chen, G., Yang, K., Li, H., Lai, Y., Litak, G., Yurchenko, D., *Hybrid wind energy scavenging by coupling vortex-induced vibrations and galloping.* Energy Conversion and

Management, 2020. **213**: p. 112835.

24. Zhu, H., Liu, W., Zhou, T., *Direct numerical simulation of the wake adjustment and hydrodynamic characteristics of a circular cylinder symmetrically attached with fin-shaped strips.* Ocean Engineering, 2020. **195**: p. 106756.
25. Yang, W.-H., Chen, W.-L., *Passive aerodynamic control of a single-box girder using self-issuing jets.* Journal of Wind Engineering and Industrial Aerodynamics, 2021. **208**: p. 104443.
26. Xu, W., Zhang, S., Ma, Y., Liu, B., Wang, J., *A study on the FIV hydrodynamic force coefficients of two staggered flexible cylinders via an inverse method.* Ocean Engineering, 2021. **219**: p. 108272.
27. Yu, H., Zhang, M., *Effects of side ratio on energy harvesting from transverse galloping of a rectangular cylinder.* Energy, 2021. **226**: p. 120420.
28. Barrero-Gil, A., Vicente-Ludlam, D., Gutierrez, D., Sastre, F., *Enhance of Energy Harvesting from Transverse Galloping by Actively Rotating the Galloping Body.* Energies, 2020. **13**(1): p. 91.
29. Sun, W., Jo, S., Seok, J., *Development of the optimal bluff body for wind energy harvesting using the synergetic effect of coupled vortex induced vibration and galloping phenomena.* International Journal of Mechanical Sciences, 2019. **156**: p. 435-445.
30. Doaré, O., Michelin, S., *Piezoelectric coupling in energy-harvesting fluttering flexible plates: linear stability analysis and conversion efficiency.* Journal of Fluids and Structures, 2011. **27**(8): p. 1357-1375.
31. Zakaria, M.Y., Al-Haik, M.Y., Hajj, M.R., *Experimental analysis of energy harvesting from self-induced flutter of a composite beam.* Applied Physics Letters, 2015. **107**(2): p. 023901.
32. Dai, H., Abdelkefi, A., Wang, L., *Theoretical modeling and nonlinear analysis of piezoelectric energy harvesting from vortex-induced vibrations.* Journal of Intelligent Material Systems and Structures, 2014. **25**(14): p. 1861-1874.
33. Achenbach, E., Heinecke, E., *On vortex shedding from smooth and rough cylinders in the range of Reynolds numbers 6× 10 3 to 5× 10 6.* Journal of fluid mechanics, 1981. **109**: p. 239-251.
34. Zdravkovich, M.M., *Flow around circular cylinders: Volume 2: Applications*. Vol. 2. 1997: Oxford university press.
35. Norberg, C., *Fluctuating lift on a circular cylinder: review and new measurements.* Journal of Fluids and Structures, 2003. **17**(1): p. 57-96.
36. Govardhan, R., Williamson, C., *Defining the'modified Griffin plot'in vortex-induced vibration: revealing the effect of Reynolds number using controlled damping.* Journal of fluid mechanics, 2006. **561**: p. 147.
37. Martins, F., Avila, J., *Effects of the Reynolds number and structural damping on vortex-induced vibrations of elastically-mounted rigid cylinder.* International Journal of Mechanical Sciences, 2019. **156**: p. 235-249.
38. Raghavan, K., Bernitsas, M., *Experimental investigation of Reynolds number effect on vortex induced vibration of rigid circular cylinder on elastic supports.* Ocean Engineering, 2011. **38**(5-6): p. 719-731.
39. Anagnostopoulos, P., Bearman, P., *Response characteristics of a vortex-excited cylinder at low Reynolds numbers.* Journal of Fluids and Structures, 1992. **6**(1): p. 39-50.
40. Zhang, M., Xu, F., Øiseth, O., *Aerodynamic damping models for vortex-induced vibration of a rectangular 4: 1 cylinder: Comparison of modeling schemes.* Journal of Wind Engineering and Industrial Aerodynamics, 2020. **205**: p. 104321.
41. Zhang, M., Xu, F., Yu, H., *A simplified model to evaluate peak amplitude for vertical vortex-induced vibration of bridge decks.* International Journal of Mechanical Sciences, 2020: p. 106145.
42. Zou, H.-X., Zhao, L.-C., Gao, Q.-H., Zuo, L., Liu, F.-R., Tan, T., Wei, K.-X., Zhang, W.-M., *Mechanical modulations for enhancing energy harvesting: Principles, methods and applications.* Applied Energy,

2019. **255**: p. 113871.

43. Facchinetti, M.L., De Langre, E., Biolley, F., *Coupling of structure and wake oscillators in vortex-induced vibrations.* Journal of Fluids and structures, 2004. **19**(2): p. 123-140.
44. Gabbai, R., Benaroya, H., *An overview of modeling and experiments of vortex-induced vibration of circular cylinders.* Journal of Sound and Vibration, 2005. **282**(3-5): p. 575-616.
45. Morse, T., Williamson, C., *Prediction of vortex-induced vibration response by employing controlled motion.* Journal of Fluid Mechanics, 2009. **634**: p. 5.
46. Zhang, M., Xu, F., Han, Y., *Assessment of wind-induced nonlinear post-critical performance of bridge decks.* Journal of Wind Engineering and Industrial Aerodynamics, 2020. **203**: p. 104251.
47. Zhang, M., Xu, F., Wu, T., Zhang, Z., *Postflutter Analysis of Bridge Decks Using Aerodynamic-Describing Functions.* Journal of Bridge Engineering, 2020. **25**(8): p. 04020046.
48. Zhao, L.-C., Zou, H.-X., Yan, G., Liu, F.-R., Tan, T., Wei, K.-X., Zhang, W.-M., *Magnetic coupling and flextensional amplification mechanisms for high-robustness ambient wind energy harvesting.* Energy Conversion and Management, 2019. **201**: p. 112166.
49. Khalak, A., Williamson, C.H., *Motions, forces and mode transitions in vortex-induced vibrations at low mass-damping.* Journal of fluids and Structures, 1999. **13**(7-8): p. 813-852.
50. Wang, J., Tang, L., Zhao, L., Hu, G., Song, R., Xu, K., *Equivalent circuit representation of a vortex‐induced vibration‐based energy harvester using a semi‐empirical lumped parameter approach.* International Journal of Energy Research, 2020. **44**(6): p. 4516-4528.
51. Zhang, M., Xu, F., *Nonlinear vibration characteristics of bridge deck section models in still air.* Journal of Bridge Engineering, 2018. **23**(9): p. 04018059.
52. Gopalkrishnan, R., *Vortex-induced forces on oscillating bluff cylinders*. 1993, WOODS HOLE OCEANOGRAPHIC INSTITUTION MA.